International Journal of Multiphase Flow 169 (2023) 104618

Contents lists available at ScienceDirect

International Journal of Multiphase Flow

journal homepage: www.elsevier.com/locate/ijmulflow

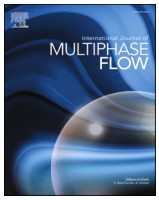

Experiments and modelling of near-horizontal bubbly flow

Jørn Kjølaas [a,*], Diana Gonzalez [a], Krister Flåten Johansen [b], Heiner Schümann [a]

[a] SINTEF Industry, Norway
[b] NTNU, Norway

ARTICLE INFO

Keywords:
Bubbly flow
Experiments
Modelling
Turbulent diffusion

ABSTRACT

This work aims to establish a fast and robust mechanistic model framework for predicting phase fraction profiles in bubbly flows. The main motivation is that the associated closure laws can in the future be used as a basis for a more general gas entrainment model in multiphase flows.

Two-phase gas-liquid experiments were conducted in a 212 meter long pipe with an inner diameter of 56.3 mm and a pipe angle of 0.13°. The experiments were conducted with Exxsol D60 oil and Argon gas. The system was pressurized to 12 bara, yielding a gas density of 19 kg/m^3. Phase fraction profiles were measured using a vertically traversing gamma densitometer, and bubble sizes were obtained using a CANTY InFlow Particle Sizer system. In addition, pressure transmitters were connected to the pipe facilitating pressure drop measurements. The experiments were performed in the bubbly flow region, where the gas was dispersed as bubbles in the liquid.

The model presented in this paper is based on a gravity/turbulent diffusion balance, where the measured bubble size distributions are used as input to the model. The agreement between the model and the data was found to be good, although some discrepancies could be seen. A key model ingredient was found to be the effect of turbulence on the bubble drag. It was also found that the Sauter mean bubble size could be used in place of the bubble size distribution without significant loss of accuracy.

1. Introduction

Bubbly flow is usually described as a gas/liquid flow regime in which the gas is in the form of small gas bubbles suspended in the liquid. Bubbly flow is important in many industrial processes, where the persistence of fully dispersed bubbly flow is needed to attain sufficiently large interfacial areas for heat and mass transfer (Andreussi et al., 1999). In this paper we consider the special case of bubbly flow in near-horizontal pipes. Maintaining bubbly flow in near-horizontal pipes requires that the flow velocity is high enough so that turbulent diffusion can counterbalance the upward gravitational drift of bubbles. Modelling bubbles in liquid in near-horizontal pipes is however challenging because the bubble distribution is a product of many complex effects related to turbulence and interaction between the bubbles.

The primary motivation for this work is related to the modelling of bubble entrainment in multiphase flows in general, with particular emphasis on flows in long pipelines. Some key application areas where bubble entrainment can be important are:

(1) Oil/gas production systems with high pressure and low surface tension. This is especially important when production chemicals that stabilize gas/liquid interfaces are deployed.
(2) Carbon Capture and Storage systems, where the conditions often facilitate bubble entrainment (Yang, 2022).

Commercially available 1D multiphase flow models such as LedaFlow (Danielson et al., 2005) include the effect of bubble entrainment at slug fronts, where gas is entrained by the highly turbulent vortices generated as the slug interacts with the slow-moving liquid film. However, gas entrainment in near-horizontal stratified flow is not modelled in LedaFlow, nor in other similar tools to our knowledge. This omission can arguably be justified in many circumstances, where the gas entrained in the liquid film is either minimal or unimportant with respect to the overall predictions. However, new measurements have shown that gas entrainment in stratified flows can be quite significant in high-pressure two-phase with pure CO_2 (Andersen et al., 2021). In such situations, the potential penalties for omitting gas entrainment in the modelling of multiphase flows include (Yang, 2022):

* Corresponding author.
E-mail address: jorn.kjolaas@sintef.no (J. Kjølaas).

https://doi.org/10.1016/j.ijmultiphaseflow.2023.104618
Received 14 April 2023; Received in revised form 14 August 2023; Accepted 14 September 2023
Available online 17 September 2023

(1) Erroneous flow regime predictions and subsequent errors in pressure drop predictions.
(2) Erroneous interfacial areas, leading to under-prediction of interfacial heat- and mass transfer.

The application areas mentioned above typically include long pipelines that cover several tens of kilometres. Simulating such systems using full 3D techniques is impractical because of the computational cost of such models. For these applications simple and robust gas bubble entrainment models are needed, and the work presented in this paper is a first step in that development.

Bubbly flow is arguably the simplest case with respect to gas entrainment. A more general scenario is one where the gas is only partially in the form of small bubbles, and partially in the form of free gas above the liquid, and the aim of this ongoing work is to ultimately develop a model that applies to the general situation. As a first step, it is however useful to start with bubbly flow because one can then ignore certain mechanism/phenomena and focus on the remaining ones that pertain to the bubble dispersion mechanics. Specifically, the following aspects are important in the general situation, but are irrelevant in bubbly flow:

(1) Gas entrainment at the gas/liquid interface, including the impact of waves and slugs.
(2) The effect of interfacial shear stress and turbulence on the turbulent diffusivity in the liquid layer.
(3) Transition between bubbly flow and other flow regimes.

In bubbly flow, the main phenomena to consider are turbulent diffusion and gravitational drift. By considering bubbly flow, we can isolate and validate the modelling of these phenomena without considering all the effects that are encountered in separated flows. The objective of this work is to derive a mechanistic model that can predict how bubbles are distributed in near-horizontal bubbly flows. This work may then serve as a basis for future work on gas entrainment in more general situations.

Modelling of near-horizontal bubbly flow has been addressed by many authors in the literature. Previous modelling efforts have mainly been performed using advanced 3D turbulence model frameworks, which require significant computational effort (Colin et al., 2000, Ekambara et al., 2008, Ekambara et al., 2012, Li et al., 2010). While these efforts have contributed much with respect to achieving a better understanding of near-horizontal bubbly flow, 3D simulations methods are in general prohibitively time consuming for the target applications of this work, which is why we attempt a simpler approach in this paper.

In the literature, bubbly flow is frequently treated as a developing flow, where the flow characteristics evolve over the covered distance (Bottin et al., 2014). This is indeed a typical scenario for many applications, especially when the pipes in question are short, where the flow in the pipe is likely to depend on the inlet boundary condition. However, in the target applications for the present work, where the pipes are long and the system pressure is high, the flow can for the most part be assumed to be fully developed. We are therefore interested in developing an equilibrium model where it is assumed that the flow is fully developed.

To our knowledge, all the bubbly flow experiments reported in the literature have been conducted at near-atmospheric conditions (Kocamustafaogullari and Wang, 1991, Kocamustafaogullari et al., 1994, Kocamustafaogullari and Huang, 1994, Bottin et al., 2014, Andreussi et al., 1999). At low pressures, the frictional pressure loss causes significant gas expansion along the pipe. The implication is that that the local volumetric gas fraction and gas flow rate increase with the distance from the inlet, calling into question whether the flow can be considered fully developed (Kocamustafaogullari and Huang, 1994). This situation is arguably not ideal for the development of steady-state equilibrium models, the premise of which is that the flow is fully developed.

To make progress on the modelling of bubbly flow, we conducted a set of gas/oil experiments in a 56.3 mm pipe at high mixture velocities (U_M>3 m/s). The system pressure was 12 bara to limit undesirable gas expansion effects along the pipe (the pressure drop over 100 meters was 1-2 bar in the experiments). Furthermore, the distance from the gas/liquid mixing point to the measurement point was around 100 meters to limit potential inlet effects. The main measurements were gas concentration profiles and bubble sizes. In Section 2.3 we will show that we detected a gradual development in the bubble size distributions, meaning that the flow was strictly speaking not at equilibrium. However, we believe that the bubble size development was sufficiently slow to assume local equilibrium, meaning that the bubble size evolution did not affect the bubble concentration profiles locally.

To predict the results obtained in the experiments we present a simple steady-state model that assumes that the fluxes due to gravitational drift and turbulent diffusion are balanced, where we include what we presume are the most important physical mechanisms for bubbly flows. The modelling approach is essentially the same as the one outlined by Yang (2022), although the closure laws used by Yang are not the same as the ones used here. The starting point of the modelling is the framework described by Kjølaas et al. (2022), which was originally developed and tested for oil/water flows. The model differs from most previously reported modelling efforts on bubbly flow in that it is simple and computationally efficient, using averaged quantities to describe the turbulent dispersion of bubbles. The model uses the measured bubble size distributions instead of a bubble size closure law. The benefit of this is that the model predictions are unhampered by uncertainties in the bubble size closure law, and that the quality of the remaining set of closure laws can be assessed. This is important because the predictions are very sensitive to the bubble sizes.

2. Experiments

The experiments were performed in a flow loop with an inner diameter of 56.3 mm. The flow loop consisted of four straight straight sections of 48 m length connected with 180° bends with 1 m bend radius. The reason for these bends was that the length of the building did not allow for straight pipes longer than around 50 meters. The total test section length was 212 meters. The pipe wall roughness k_S was estimated to be about 2 μm based on flow experiments with only liquid. A small pipe inclination of 0.13° was introduced to allow for sufficient spacing between the pipe sections to allow for mounting the traversing gamma densitometers. For the experiments described in this paper, the flow velocities are so high that the pipe inclination has no practical significance. The experimental setup is illustrated in Fig. 1. The distance from the inlet to the measurements emphasized in this paper was about 100 meters. The associated instruments are enclosed in the red dashed ellipse in Fig. 1. Exxsol D60 (density 789 kg/m^3 and viscosity 1.3 cP) was used as the liquid phase, and the gas phase was Argon pressurized to 12 bara, yielding a density of 19 kg/m^3. The fluid temperatures were in the range 23-37°C. All the experiments were conducted with a superficial liquid velocity *USL* of 3 m/s, while the superficial gas velocity *USG* was varied from 0.2 to 1.9 m/s. The flow was fully turbulent for all the cases presented here, with Reynolds numbers exceeding 10^5.

The flow loop was instrumented with pressure sensors, traversing gamma densitometers are labelled, and a bubble size measurement system. The locations of these instruments are listed in Table 1, and descriptions of the measurements are included in Sections 2.2, 2.3, and 2.4. The traversing gamma densitometer enclosed in the red dashed ellipse in Fig. 1 is the one used in this paper.

It should be noted that the flow goes through a 180° bend at the halfway point to the 100-meter mark. Although having such a bend is not ideal, we do not believe that this bend should have a significant impact on the flow 50 meters downstream. Indeed, calculations presented in Section 3.4 indicate that the relaxation time for the flow should be in the order of one second or less, leading us to believe that any adverse effects

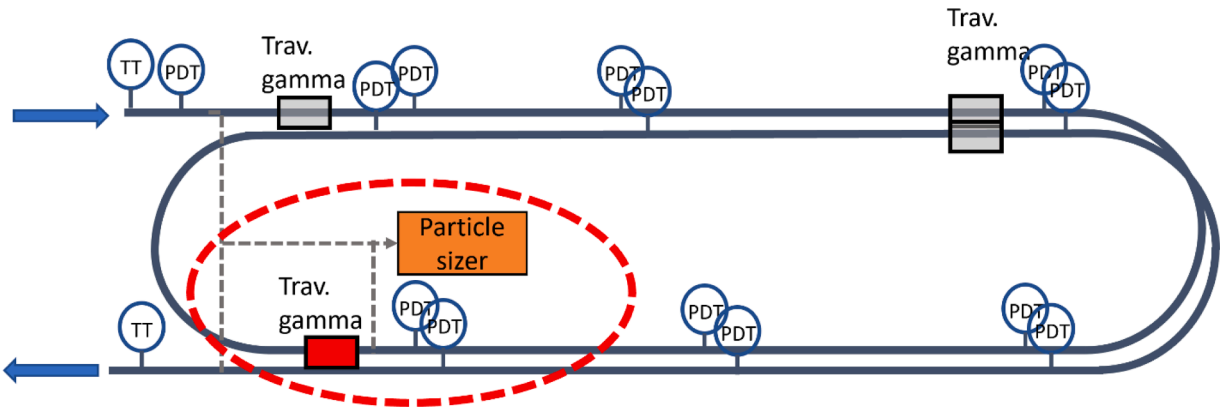

Fig. 1. Illustration of the experimental setup. Pressure transmitters are labelled as "PDT", Temperature transmitters are labelled "TT", traversing gamma densitometers are labelled "Trav. Gamma", and the bubble size measurement system is labelled "particle sizer". The gray dashed lines show where the bubble measurement apparatus was connected to the pipe.

Table 1
Instrument positions

Instrumentation	Position [m]
Pressure transducers	2.17, 12.62, 26.68, 49.25, 56.71, 78.28, 100.15, 108.19, 130.77, 153.33, 160.78, 182.33, 204.21
Temperature transmitters	0.1, 211
Traversing gamma densitometers	0.74, 47.39, 102.40, 151.46
Droplet sampling probes	2.43, 100.57, 209.50

on the gas bubble distribution introduced by the bend should dissipate long before the main measurement point.

2.1. Flow measurements and densities

The gas- and liquid mass flow rates were measured using Coriolis meters, and the respective uncertainties should be better than 1% of the measured values. The superficial gas and liquid velocities *USG* and *USL* were obtained by dividing the mass flow rates by the pipe cross section area and the respective fluid densities (Table 2).

The liquid density values were obtained from the Coriolis meter on the liquid line, while the gas density was based on interpolating tabulated values from NIST (NIST, 2023) Because the gas density depends on the pressure, the superficial gas velocity increases somewhat along the test section. The values that we have reported in this paper are those obtained at 100 meters from the inlet. These values were obtained by interpolating the pressure- and temperature measurements and calculating the local gas density at 100 meters accordingly. The volumetric mixture velocity U_M is simply the sum of the superficial liquid- and gas velocities.

2.2. Pressure measurements

The pressure measurements were used to calculate the pressure drop at various locations along the test section by dividing the pressure differences by distance between the sensors. The results of this analysis are shown in Fig. 2, where we have plotted the pressure drop versus distance from the inlet for each of the experiments. We have in this figure

Table 2
Fluid properties

Phase	Viscosity [cP]	Density [kg/m^3]	Surface tension [mN/m]
Oil	1.3	789	19.0
Gas	0.02	19	

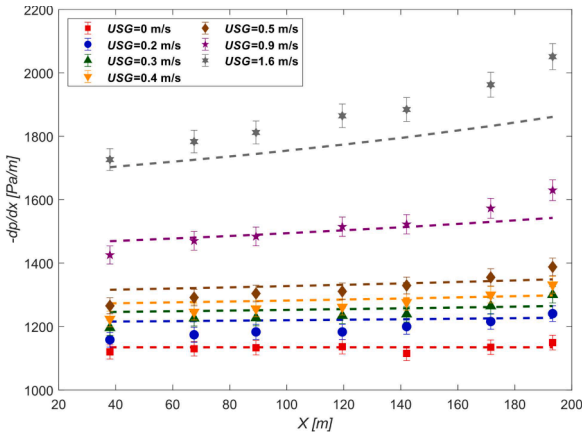

Fig. 2. Pressure drop plotted versus distance form the inlet. The markers represent measured values, and the dashed lines represent calculations assuming homogeneous flow assumptions.

included results for single phase liquid flow (red squares) in addition to the two-phase experiments. We have excluded the two first pressure sensors from these calculations because they were suspected to be influenced by entrance effects (the associated pressure gradient measurements deviated somewhat from the values obtained downstream). Also, we do not show the pressure gradients measured over the pipe bends because of the associated centrifugal forces.

The dashed lines in Fig. 2 represent pressure drop calculations where we have assumed homogeneous flow:

$$-\frac{dp}{dx} = \frac{2 \cdot f \rho_M U_M^2}{D} + \rho_M g \sin\phi \tag{1}$$

Here, ρ_M is the mixture density, which we estimate using the assumption of no-slip:

$$\rho_M = \frac{USG \cdot \rho_G + USL \cdot \rho_L}{USG + USL} \tag{2}$$

We note here that the values of USG and ρ_G are calculated locally using the pressure measurements so that the effect of gas expansion is included. The friction factor f is calculated using the Håland formula (Håland, 1983)

$$\frac{1}{\sqrt{f}} = -\log_{10}\left[\frac{6.9}{\mathrm{Re}_M} + \left(\frac{k_S}{3.7D}\right)^{1.11}\right] \tag{3}$$

where the mixture Reynolds number Re_M was been defined as:

$$\mathrm{Re}_M = \frac{\rho_M D U_M}{\mu_L} \tag{4}$$

We observe that the above assumptions yield reasonable results for most of the scenarios. For the highest gas rate (*USG*=1.6 m/s), we do however observe some notable deviations, where the calculations under-predict the measured values significantly.

2.3. Bubble size measurements

Bubble sizes were measured using a particle-sizing camera (CANTY InFlow™) located 100 meters from the inlet. The sampling tubes had an inner diameter of 8 mm and were oriented opposite to the flow direction. The sampling tube was traversed in the vertical direction, yielding bubble size distributions at three vertical positions (8 mm from the top, at the pipe center, and 8 mm from bottom). The rubber hose connecting the sample points with the particle sizing camera was 5 meters long, and had an inner diameter of 9 mm. The flow itself through the sampling tubes was adjusted using hand operated control valves to attain a flow velocity between 1 and 2 m/s. From the particle sizing camera, the fluids were routed back into the separator. The bubbles were measured and counted using a combination of manual counting and a machine learning algorithm based on a TensorFlow object identification algorithm. For each experiment, around 3500 bubbles were recorded, and 70% of the bubbles in each experiment were counted manually. The manually counted bubbles were used to train an object detection algorithm, which was then used to count the remainder of the bubbles. The Sauter mean diameters obtained with the machine learning algorithm deviated from the manual counting by less than 0.1%.

The top graph in Fig. 3 shows the measured cumulative volume-weighted bubble size distributions. Here, the droplet sizes from all three vertical sampling positions are included. The bottom graphs in Fig. 3 shows the Sauter mean bubble diameter plotted versus the superficial gas velocity *USG*. The Sauter mean bubble diameter $d_{B,32}$ is the area-weighted bubble diameter, and is defined as:

$$d_{B,32} = \frac{\langle d_B^3 \rangle}{\langle d_B^2 \rangle} \tag{5}$$

where d_B represents the measured bubble diameter distribution for all

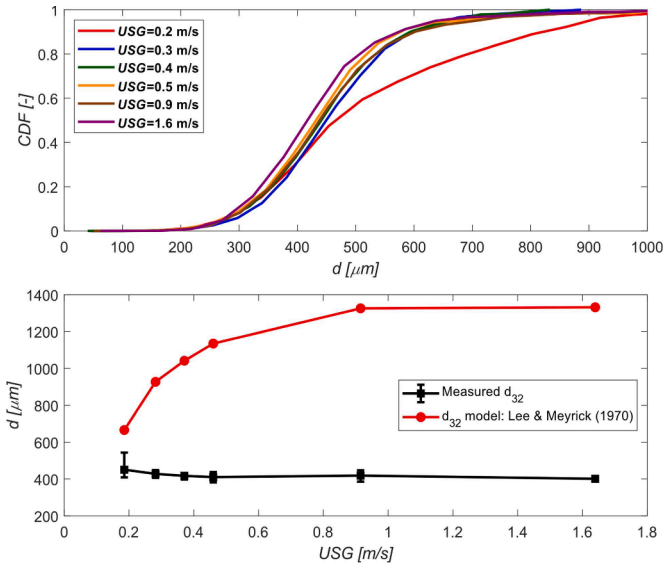

Fig. 3. Top graph: Cumulative volume-weighted bubble size distributions based on data from al the three vertical sampling positions. Bottom graph: Sauter mean bubble diameter and the Lee & Merick model plotted versus *USG*. The error bars associated with the black squares show the maximum and minimum values found among the three vertical positions.

three vertical sampling positions. The error bars in the second graph represent the maximum and minimum Sauter mean values measured at the various vertical positions. Here, the maximum values were always at the top, and the minimum values were always at the bottom. The red markers in this graph represents values obtained using a model proposed by Lee and Meyrick (1970) based on data from impeller-agitated reactors:

$$d_{B,32} = 4.25\sqrt{\alpha_g}\left(\frac{\sigma}{\rho}\right)^{0.6}\varepsilon^{-0.4} \tag{6}$$

Here, α_g is the volumetric gas fraction (cross-section average), σ is the gas/liquid surface tension, ρ is the liquid density, and ε is the energy dissipation rate. The energy dissipation rate was calculated using the measured frictional pressure drop dp/dx_{fric}, the volumetric mixture velocity U_M, and the mixture density ρ_M:

$$\varepsilon = \frac{U_M}{\rho_M}\cdot\left|\frac{dp}{dx}\right|_{fric} \tag{7}$$

We observe that the measured Sauter mean bubble sizes are quite similar for all the experiments, and they are significantly lower than the values obtained from the model proposed by Lee and Meyrick (1970). It should however be noted that the bubble sizes measured in the flow experiments were found to be affected by the inlet mixing point (T-junction). This is shown in Fig. 4, where we have plotted the Sauter mean bubble diameter versus the distance from the mixing point. Presumably, the shearing forces in the T-junction were higher than in the flow downstream, leading to bubbles that were smaller than the equilibrium value. This would explain the trends seen in Fig. 4, where the bubble size increases with distance from the inlet.

In the present work, we have chosen to use the measured bubble sizes as model input rather than implementing a bubble size model. If the gas bubble concentration profile evolves sufficiently fast compared to the bubble sizes, we can assume local equilibrium, and the origin of the prevailing bubble sizes is not a major concern. The time scale for the gas bubble distribution was estimated by dividing the pipe diameter by the bubble settling velocity (see Section 3.3), and the resulting values were less than one second for all the cases. Based on the results shown in Fig. 4, we found that the Sauter mean bubble diameter increases less than 5 μm during that time (around 1%), which is arguably negligible. Consequently, we believe that we can assume local equilibrium, which is one of the premises of the model outlined in this paper.

The residence time of the bubbles inside the rubber hose was in the range 2.5-5 seconds, and the associated Reynolds number range would have been around 5 000-10 000. One concern with this setup was that the bubble sizes inside the hose might have evolved on the way through, meaning that the measured sizes were not entirely representative of the bubbles inside the pipe. It was unfortunately not possible to check the degree of bubble break-up/coalescence taking place inside the hose. However, given that the Reynolds numbers in the hose were substantially lower that those encountered in the pipe, we can probably rule out bubble break-up in the hose. The coalescence rate inside the hose might however have been non-zero. Still, we would expect the coalescence rate inside the hose to be lower than that inside the pipe because of the relatively low Reynolds numbers in the hose. Specifically, the relative velocity between the bubbles would have been lower than in the pipe, yielding a lower collision frequency, and consequently a lower coalescence rate (Liao and Lucas, 2010) In the worst-case scenario, where the coalescence rate in the hose equals that in the pipe, and the velocity in the hose is 1 m/s, the increase in the Sauter mean bubble size in the hose would have been about 6%. Using the model outlined in Section 3, we found that a bubble size increase of 6% did not have an appreciable effect on the predictions, hence we concluded that this experimental uncertainty did not affect the findings of this paper.

2.4. Traversing gamma densitometers

Several traversing gamma beam densitometers were installed on the test section to measure density profiles, but in this paper we consider only the gamma densitometer located 100 meters downstream of the inlet. The gamma densitometer used a Caesium 137 radiation source combined with a Sodium Iodide scintillator. The gamma densitometer was calibrated by measuring count rate profiles in pure gas and pure liquid, where the fluid densities were known. The logging frequency was 50 Hz, and the traversing velocity was 0.2 mm/s. The resulting gas concentration profiles for the various experiments are shown in Fig. 4.

The gamma densitometer data has two main sources of error: stochastic noise from the radiation process, and miscellaneous systematic errors with unknown origins (instrument drift, scattered photons reaching the scintillator, etc.). The stochastic component has a standard deviation of about 0.01, and the systematic contribution was estimated to 0.01.

Fig. 6 shows the average gas fraction measured by the traversing gamma densitometer plotted versus the superficial gas velocity *USG*. The blue dashed line represents the no-slip gas fraction, which is the prevailing gas fraction in the case where the gas and liquid travel at the same average velocity:

$$\alpha_G^{\text{no-slip}} = \frac{USG}{USG + USL} \tag{8}$$

We observe that the measured gas fractions are slightly lower than the no-slip values, implying that the gas travels faster than the liquid. We must however point out that the deviations from no-slip are only barely larger than two standard deviations of measurement uncertainty. This means that the measured slip velocities may be partially caused by measurement error and should therefore be interpreted with caution.

3. Modelling

To model the bubble concentration profiles shown in Fig. 5, we use the model framework presented by Kjølaas et al. (2022). The model is a simple steady-state gravity/diffusion balance equation, which is a common approach for modelling particle transport in general (Kjølaas et al., 2022, Skartlien, 2009, Skartlien et al., 2011):

$$\varepsilon_B \frac{dC}{dy} + C \cdot U_T(C) = 0 \tag{9}$$

In equation, C represents the volumetric bubble concentration, y is the vertical distance from the pipe bottom, ε_B is the bubble diffusivity, and U_T is the settling velocity of the bubbles relative to the liquid. The first term in equation represents the average flux of bubbles caused by turbulent diffusion, and the second term represents the bubble flux due to gravity. The model is described in detail by Kjølaas et al. (2022), but we will for the sake of completeness include a description of this model here as well.

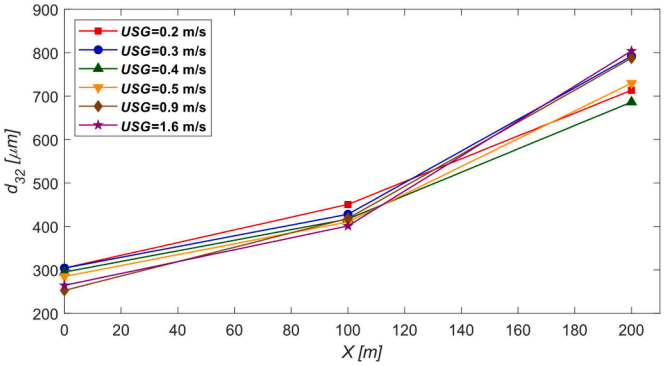

Fig. 4. Sauter mean bubble size plotted versus the distance form the inlet.

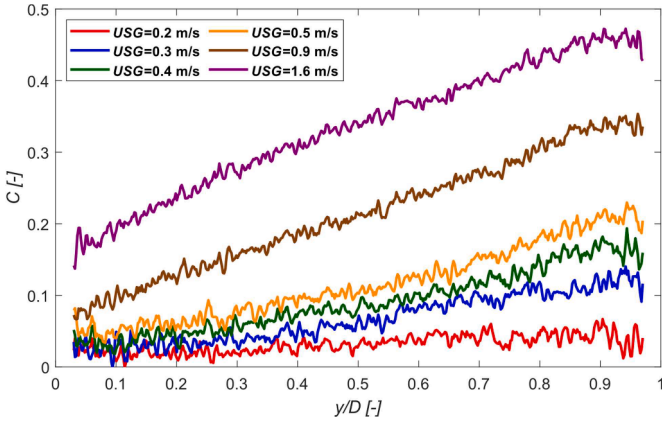

Fig. 5. Gas concentration profiles obtained using the traversing gamma densitometer. The parameter y represents the distance from the pipe bottom.

The model described by Kjølaas et al. (2022) was originally developed for dispersed oil/water flows and was validated accordingly. Still, the physical mechanisms and closure laws included in that model are in principle applicable to other types of systems, hence one might expect that model to be sufficiently general to apply to for bubbly flows as well. In this paper we will show that this model does indeed work well for bubbly flows, provided that we include the effect of added mass, which is the effect of the surrounding fluid of the bubbles' effective inertia (see Section 3.4). The effect of added mass was not included in the original model because this effect was found to be negligible in oil/water flows. The effect of added mass can however be very important in scenarios where the particle/fluid density ratio is low, which is typically the case for gas/liquid bubbly flows.

The gravitational drift of the bubbles (the terminal velocity U_T) is highly dependent on the bubble size. Equivalent to the oil/water modelling work (Kjølaas et al., 2022), we here use the measured bubble size distributions as input to the model instead of introducing a bubble size closure law. This allows us to evaluate some of the core model elements without being unduly hampered by uncertainties in the bubble size model. A fully predictive model would of course require a closure law for the bubble sizes, but this has not been addressed here.

In this model we assume that the flow regime is bubbly flow, meaning that the gas is entirely in the form of bubbles dispersed in the liquid, which is the case for all the experiments included in this analysis. Also, like Kjølaas et al. (2022), we assume that the gas concentration does not vary in the lateral direction.

3.1. Mass conservation

In Fig. 6 it was shown that the average slip velocity between the gas bubbles and the liquid was non-zero, the gas bubbles travelling slightly faster than the liquid. We presently do not know the reason for this non-zero slip velocity, and this lack of understanding prevents us from proposing/deriving a physical model for predicting this phenomenon. Still, the objective of this work has been to establish a model framework for predicting the vertical dispersion of bubbles in horizontal flows, and this process is to a great extent independent of the axial slip. It should be noted that local axial gas-liquid slip can play a role in the vertical dispersion through the lift force (Saffman, 1965). However, in (Kjølaas et al., 2022) it was argued that this effect only influences the near-wall behaviour, and should therefore not be very important for the prediction of the concentration profile away from the walls. Regardless, we have elected to ignore the modelling axial gas-liquid slip, and simply impose the condition that the total predicted gas volume fraction must equal the measured value:

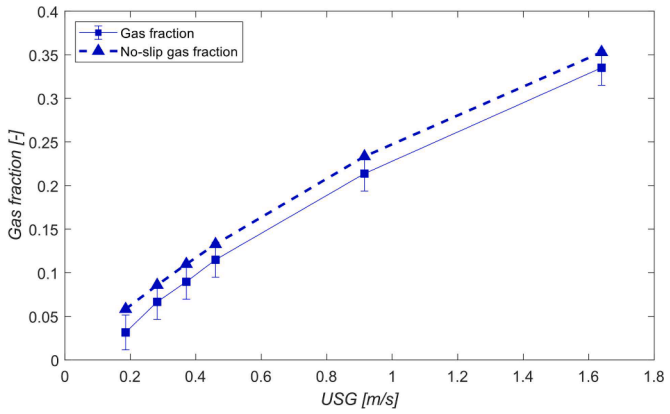

Fig. 6. Square markers: measured gas fraction plotted against the superficial gas velocity USG. Triangles: The no-slip gas fraction: USG/(USL+USG). The error bars represent two standard deviations.

$$\frac{1}{A}\int_0^D C(y)dA = \alpha_G^{meas} \tag{10}$$

This is equivalent to imposing the measured gas-liquid slip as input to our model. The justification for using this approach is that we wanted to isolate and assess the dispersion model framework without any concerns about the axial slip. In a fully predictive model, this condition should ideally be replaced by a model for the axial gas-liquid slip velocity combined with a mass conservation equation for the gas. An adequate approach here may be to simply assume zero slip between the gas and liquid, since the measured deviations from no-slip are relatively small.

3.2. Eddy diffusivity

The bubble dispersion process is driven by the turbulent eddies. For single phase turbulent pipe flow, the eddy diffusivity is relatively well understood. There are several models for the local eddy diffusivity ε_F in single phase pipe flow, but they are generally quite similar. The model derived by Reichhardt (1951) is one example:

$$\frac{\varepsilon_F}{R\cdot U*} = \frac{\kappa}{3}\left(\frac{1}{2}+r^2\right)\left(1-r^2\right) \tag{11}$$

where r is the distance from the pipe centre, R is the radius of the pipe, κ is the von Karman constant ($\approx$0.41), and U^* is the average friction velocity:

$$U* = \sqrt{\frac{\tau_{avg}}{\rho_M}} = \sqrt{\frac{D\cdot|dp/dx|_{fric}}{4\rho_M}} \tag{12}$$

In Eq. (12) τ_{avg} is the average wall shear stress, ρ_M is the average mixture density, and dp/dx_{fric} is the frictional pressure gradient (measured using pressure transmitters 5, 6 and 7). It was shown by Kjølaas et al. (2022) that this detailed diffusivity model can be substituted by a constant dimensionless diffusivity of 0.07 with little to no adverse effects on the overall accuracy. This corresponds to replacing the entire right-hand-side of equation with 0.07. We have therefore elected to do so in this work.

We should point that in principle, the bubble diffusivity ε_B is not necessarily the same as the eddy diffusivity ε_F. However, as pointed out by Kjølaas et al. (2022), the assumption that these two parameters are the same is a reasonable approximation for most scenarios.

3.3. Gravitational drift

By formulating a force balance on a bubble considering the effects of gravity, buoyancy and drag, the terminal velocity U_T of a bubble suspended in a fluid with density ρ_F, with diameter d_B and density ρ_B is given by:

$$U_T^2 = \frac{4d_B g_y(\rho_F-\rho_B)}{3C_D\rho_F} \tag{13}$$

Here, $g_y = g\cos\phi$ is the gravity acceleration in the direction normal to the flow (ϕ being the pipe angle relative to the horizontal), and C_D is the bubble drag coefficient. In this paper we use the same drag coefficient model as Kjølaas et al. (2022), which is the model presented by Clift and Weber (1988):

$$C_D = 24\frac{1+0.15\mathrm{Re}_D^{0.687}}{\mathrm{Re}_D} \tag{14}$$

In Eq. (14), Re_B is the bubble Reynolds number, which is defined as:

$$\mathrm{Re}_B = \frac{\rho_F d_B U_T}{\mu_F} \tag{15}$$

Here, μ_F is the liquid viscosity. So far we have considered the situation where bubbles do not interact with each other, which would be the case for dilute systems. In systems densely populated with bubbles, the terminal velocity given by the equations above will typically be too high, because bubble-bubble interactions tend to impede the motion of the bubbles. This phenomenon is referred to as "hindrance". The effect of hindrance was investigated experimentally by Richardson and Zaki (1954), who based on their data proposed an empirical formula expressing the hindrance effect:

$$U_T = U_{T0}\cdot(1-C)^n \tag{16}$$

In equation U_{T0} is the terminal velocity for a dilute system, and n is the so-called hindrance parameter, which depends on the particle/bubble Reynolds number Re_B (equation). As suggested by Kjølaas et al. (2022), we use the expression proposed by Rowe (Rowe, 1987) to calculate the hindrance parameter n, since it is virtually equivalent to the more complex expression originally provided by Richardson and Zaki (1954):

$$n = \frac{4.7+2.35\cdot K}{1+K} \tag{17}$$

Here, the parameter K is defined as:

$$K = 0.175\cdot\mathrm{Re}_B^{0.75} \tag{18}$$

As pointed out by Kjølaas et al. (2022), equation gives the settling velocity of a cloud of particles in a tank in the laboratory reference frame. In that setting, the observed particle velocity is partly a result of liquid displacement, where the particle settling causes the surrounding liquid to move in the opposite direction. In the system that we are considering, there is no such displacement effect, hence equation must be modified accordingly. To this end, Kjølaas et al. (2022) showed that the correct expression for the hindered settling velocity in our setting is:

$$U_T = U_{T0}\cdot(1-C)^{n-1} \tag{19}$$

3.4. The effect of turbulence on the bubble drag

Kjølaas et al. (2022) showed that to accurately predict the dispersion of water droplets in oil, the effect of turbulence on the droplet settling velocity must be accounted for. In this paper we will show that the same is true for bubbles in liquid, which is why we include this effect in the present model as well. The total instantaneous drag force $\vec{F}_D$ on the bubbles is given by:

$$\vec{F}_D = \frac{1}{2}\rho_F C_D A_B\left|\vec{U}_B-\vec{U}_F\right|\left(\vec{U}_B-\vec{U}_F\right) \tag{20}$$

Here, A_B is the bubble cross section area, $\vec{U}_B$ and $\vec{U}_F$ are the

instantaneous bubble- and fluid velocity vectors. By substituting Eq. (14) and, into Eq. (20), we obtain:

$$\overrightarrow{F}_D = \frac{12\mu_F A_B}{d_B}\left(1+0.15\left(\frac{\rho_F d_B\left|\overrightarrow{U}_B-\overrightarrow{U}_F\right|}{\mu_F}\right)^{0.687}\right)\left(\overrightarrow{U}_B-\overrightarrow{U}_F\right) \tag{21}$$

The average drag force $\langle F_D\rangle$ in the vertical direction is then:

$$\langle F_D\rangle = \frac{12\mu_F A_B}{d_B}\left(\langle u_B-u_F\rangle+0.15\left(\frac{\rho_F d_B}{\mu_F}\right)^{0.687}\left\langle\left|\overrightarrow{U}_B-\overrightarrow{U}_F\right|^{0.687}(u_B-u_F)\right\rangle\right) \tag{22}$$

Here we have defined $u_B$as the vertical component of the instantaneous bubble velocity, and u_F as the vertical component of the instantaneous liquid velocity. Here, $\langle u_B - u_F\rangle$ simply represents the average drift velocity U_{T0}, while the expression $\langle|\overrightarrow{U}_B-\overrightarrow{U}_F|^{0.687}(u_B-u_F)\rangle$ requires some attention. To this end, we start by examining the averaged squared slip velocity:

$$\left\langle\left(\overrightarrow{U}_B-\overrightarrow{U}_F\right)^2\right\rangle = \left\langle\overrightarrow{U}_B^2\right\rangle+\left\langle\overrightarrow{U}_F^2\right\rangle-2\left\langle\overrightarrow{U}_B\cdot\overrightarrow{U}_F\right\rangle \tag{23}$$

We now decompose the instantaneous bubble velocity vector into a mean value U_{T0}, and three fluctuating components (one for each direction) with magnitude u' and a mean value of zero:

$$\overrightarrow{U}_B = [U_X+u',U_{T0}+u',u'] \tag{24}$$

Here, U_X represents the local ensemble-averaged velocity in the flow direction. We treat the instantaneous fluid velocity in the same way, allowing the vertical fluid velocity component u_F (which has a mean value of zero) to represent the fluctuating component:

$$\overrightarrow{U}_F = [U_X+u_F,u_F,u_F] \tag{25}$$

Here we have assumed that the bubbles and the liquid travel at the same axial velocity U_X. We should note here that the experimental data suggests that this is not the case, since measurements show that the average gas velocity is higher than the averaged liquid velocity. However, we do not have any local measurements of the gas-liquid slip, hence it is difficult to introduce a more sophisticated model than zero axial slip. This is however a potential weakness in the model, possibly leading to discrepancies between the predictions and the measurements. Regardless, with the assumption of no axial slip we obtain (exploiting that $\langle u'\rangle = \langle u_F\rangle = 0$):

$$\left\langle\left(\overrightarrow{U}_B-\overrightarrow{U}_F\right)^2\right\rangle = U_{T0}^2+3\langle u'^2\rangle+3\langle u_F^2\rangle-6\langle u'u_F\rangle \tag{26}$$

We now use the "locally homogeneous approximation" (Skartlien, 2009), where we assume that the turbulence is locally homogeneous. As derived by Skartlien (2009) and Pourahmadi (1982), this assumption leads to:

$$\langle u'^2\rangle \approx \frac{\langle u_F^2\rangle}{1+St} \tag{27}$$

$$\langle u'u_F\rangle \approx \frac{\langle u_F^2\rangle}{1+St} \tag{28}$$

As suggested by several authors (Kjølaas et al., 2022, Hay et al., 1996, Pan and Hanratty, 2002), we approximate the fluid velocity fluctuations $\langle u_F^2\rangle$(in one dimension) by:

$$\langle u_F^2\rangle = (0.9\cdot U*)^2 \tag{29}$$

where U^* is the average friction velocity. The Stokes number St is defined as the ratio between the bubble relaxation time scale τ_B and the integral turbulence time scale τ_F. The bubble relaxation time τ_D can be calculated as (Lee et al., 1989, Pan and Hanratty, 2002):

$$\tau_B = \frac{\left(\rho_B+\frac{1}{2}\rho_F\right)U_{T0}}{\Delta\rho\cdot g_y} \tag{30}$$

Here we have included the effect of added mass (van Wijngaarden, 1976), where the inertial density of the bubbles represented by ρ_B has been replaced by $\rho_B+\rho_F/2$. For gas bubbles, the added mass represents the main contribution of the effective inertial mass and is thus the main factor in terms of increasing the bubble relaxation time.

We calculate the integral turbulence time scale τ_F from the average eddy diffusivity ε_F (Skartlien, 2009):

$$\tau_F = \frac{\varepsilon_F}{\langle u_F^2\rangle} \tag{31}$$

By substituting Eqs. (27) and (28) into (26), we obtain the following expression for the average squared slip velocity:

$$\left\langle\left(\overrightarrow{U}_B-\overrightarrow{U}_F\right)^2\right\rangle = U_{T0}^2+\frac{3\langle u_F^2\rangle}{1+St}+3\langle u_F^2\rangle-\frac{6\langle u_F^2\rangle}{1+St} = U_{T0}^2+\frac{3\langle u_F^2\rangle St}{1+St} \tag{32}$$

This expression shows that the instantaneous slip velocity may be considered as the sum of a mean component with magnitude U_{T0}, (in the vertical direction) and a fluctuating component with a variance $3\langle u_F^2\rangle St/(1+St)$. If we assume that the velocity fluctuations u_F follow a Gaussian distribution, we can evaluate the expression $\langle|\overrightarrow{U}_B-\overrightarrow{U}_F|^{0.687}(u_B-u_F)\rangle$ by numerically integrating the following expression:

$$\left\langle\left|\overrightarrow{U}_B-\overrightarrow{U}_F\right|^{0.687}(u_B-u_F)\right\rangle = \frac{1}{\sqrt{2\pi\sigma^2}}\int_{-\infty}^{\infty}|x|^{0.687}x\cdot\exp\left(\frac{-(x-U_{T0})^2}{2\sigma^2}\right)\cdot dx \tag{33}$$

Here, we have defined the variance σ^2 as:

$$\sigma^2 = 3\langle u_F^2\rangle\frac{St}{1+St} = 3\cdot(0.9\cdot U*)^2\frac{St}{1+St} \tag{34}$$

We can now calculate U_{T0} from the bubble force balance:

$$\frac{12\mu_F}{d_B}\frac{\pi d_B^2}{4}\left(\langle u_B-u_F\rangle+0.15\left(\frac{\rho_F d_B}{\mu_F}\right)^{0.687}\left\langle\left|\overrightarrow{U}_B-\overrightarrow{U}_F\right|^{0.687}(u_B-u_F)\right\rangle\right) = \frac{\pi d_B^3(\rho_F-\rho_B)g_y}{6} \tag{35}$$

This expression can be re-arranged to:

$$\langle u_B-u_F\rangle+0.15\left(\frac{\rho_F d_B}{\mu_F}\right)^{0.687}\left\langle\left|\overrightarrow{U}_B-\overrightarrow{U}_F\right|^{0.687}(u_B-u_F)\right\rangle = \frac{g_y d_B^2(\rho_F-\rho_B)}{18\mu_F} \tag{36}$$

Substituting $\langle u_B - u_F\rangle = U_{T0}$ and Eq. (33) into equation, we get:

$$U_{T0}+0.15\left(\frac{\rho_F d_B}{\mu_F}\right)^{0.687}\cdot\frac{1}{\sqrt{2\pi\sigma^2}}\int_{-\infty}^{\infty}|x|^{0.687}x\cdot\exp\left(\frac{-(x-U_{T0})^2}{2\sigma^2}\right)\cdot dx = \frac{g_y d_B^2(\rho_F-\rho_B)}{18\mu_F} \tag{37}$$

Equation can easily be solved for U_{T0} through iterative successive substitution.

3.5. Solving the bubble concentration model

The solution algorithm used here is the same as the one described in Kjølaas et al. (2022), but we include a brief description of it below for completeness. Since we integrate equation from the pipe top and down to the pipe bottom, we use the bubble size distributions measured near

the top of the pipe as model input.

The bubble size distributions were divided into 15 bins with the same width, where we defined the normalized volume of bubbles in each bin i as p_i. In other words, p_i represents the volume fraction of bubbles at the pipe top represented by bin i.

When solving the equation system, it is assumed that the bubbles do not coalescence or break. With this assumption, the gravity/diffusion equation for bubble size bin i can be formulated as:

$$\varepsilon_B(y)\frac{dC_i(y)}{dy} + C_i(y)\cdot U_{T0,i}\cdot\left(1-\sum_j C_j(y)\right)^{n-1} = 0 \tag{38}$$

The boundary conditions for equation i is:

$$C_i(y=0) = p_i C_0 \tag{39}$$

where C_0 is the total concentration at the top of the pipe (which is initially unknown). The algorithm used to solve this equation system is outlined in Kjølaas et al. (2022).

4. Results and discussion

4.1. Predictions with the full model

Fig. 7 shows the predicted gas concentration profiles obtained using the model outlined in Section 3 (thick lines) along with the respective measurements (thin lines). We find that the comparison between the predictions and the measurements is generally quite satisfactory, although we do observe some deviations. Specifically, we observe that the predicted profiles are a bit too heterogeneous (too large concentration gradient) for the lowest gas rates, and slightly too homogeneous (too small concentration gradient) for the highest gas rate. This suggests that the model might be lacking some physical mechanisms, or that one or more of the applied assumptions are not accurate.

Some physical mechanisms that we have omitted in our model include lift forces (Saffman, 1965), particle-wall collisions (Sommerfeld, 1992, Tian, 2006), turbophoresis (Reeks, 1983), and granular pressure (v. Wachem et al., 2001, Gidaspow, 1994, Laux, 1998). However, since these mechanisms are confined to the near-wall regions, where the velocity gradient is high, we do not believe that including such effects would substantially improve the predictions.

As pointed out by Kjølaas et al. (2022), the empirical hindrance model, which was developed for fluidised beds, might be partially responsible for some of the deviations. Inadequacies in the hindrance model would however be expected to be of little importance for small gas volume fractions. Since we do observe model discrepancies for the lowest gas flow rates, it seems that the model discrepancies cannot be attributed to the hindrance model alone.

As highlighted in Section 3.4, we have in our model assumed that the local axial gas-liquid slip velocity is zero, which according to the data is not entirely correct. We do however not have any local measurements of the gas-liquid slip velocity, and the measured average slip velocities are arguably not accurate enough to be used to estimate the local slip. Nonetheless, we suspect that the lack of a slip velocity model may partly be the cause of some of the discrepancies between the model and the data. Specifically, some exploratory testing revealed that by introducing a global slip velocity of 7% of the mixture velocity gave a near-perfect match for the four lowest gas rates.

For the highest gas flow rate (USG=1.6 m/s) we observe that the predicted profile is flatter than the measured profile. In this case, the introduction of gas/liquid slip would not help, it would in fact make matters worse. This discrepancy might be related to our assumption that the turbulence not modified by the bubbles. Specifically, one might imagine that high concentrations of bubbles suppresses the turbulent velocity fluctuations, and thereby the turbulent diffusivity. However, accounting for turbulence modulation is far from straightforward (Kenning and Crowe, 1997), especially in the simple model framework applied here, hence we have elected to forego this matter for now.

4.2. The importance turbulence on the drag force

In Section 3.4 we introduced the effect of turbulence on the average drag force on particles. This effect is sometimes omitted/overlooked in computational models for dispersed flows (Ruth et al., 2021). In this section we examine the importance of including this effect for the experiments presented in this paper. Fig. 8 presents measurements and predictions of gas concentration profiles for two of the cases included in Fig. 7 (USG=0.5 and 0.9 m/s). The thick black lines represent the measured profiles, and the blue lines represent the full model as described in Section 3. The green dotted lines show the results obtained while omitting the effect of turbulence on the drag force (Section 3.4). We observe that those results deviate quite significantly from the full model, and more importantly the experimental data, showing that incorporating the effect of turbulence on the drag force is quite crucial in

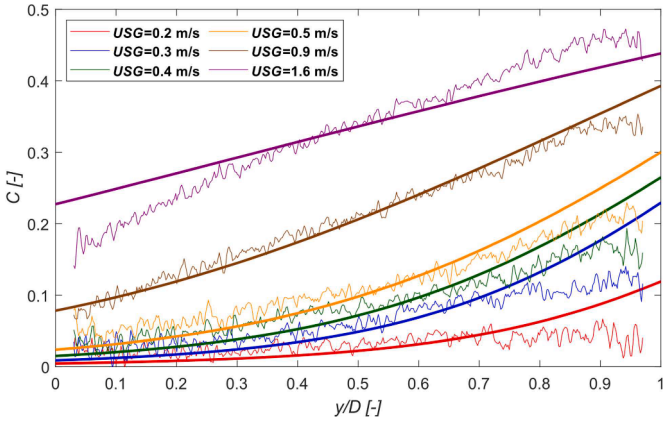

Fig. 7. Measured and predicted volumetric gas concentration profiles for USL=3 m/s and USG=0.2-1.6 m/s. The parameter y represents the distance from the pipe bottom. The thin lines represent the measurements, and the thick lines represent the model predictions.

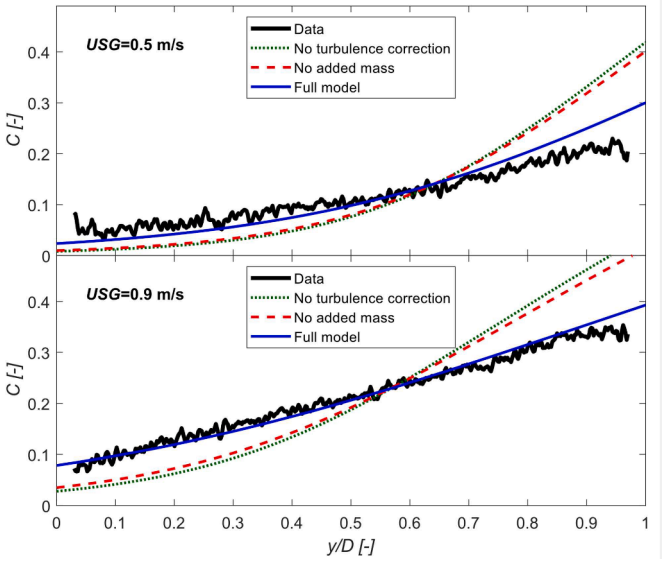

Fig. 8. Examples (USG=0.5 and 0.9 m/s) showing the importance of accounting for turbulence on the drag force. The black lines represent measured data, the blue lines are model predictions obtained using the full model, the green dotted lines are model predictions without the turbulence correction to the drag force, and the red dashed lines are model predictions without the added mass effect.

these scenarios. The red dashed lines were obtained by including the effect of turbulence on the drag force, but ignoring the effect of added mass (see Eq. (30)). These predictions are very similar to those obtained when omitting the effect of turbulence all together. In other words, including the effect of added mass is absolutely necessary.

4.3. Using the Sauter mean bubble diameter

The overall objective of this work was to derive a simple and efficient model for predicting gas concentration profiles in bubbly flows. In the model outlined in Section 3, we used the measured bubble size distributions as input to the model. There are two main problems with using bubble size distributions:

(1) The calculations become computationally heavy because many equations must be solved simultaneously, which goes against the ambition of deriving an efficient model.
(2) Ultimately, in a truly predictive model, the bubble sizes must be predicted, not measured. Predicting bubble size distributions is however difficult, which negates the ambition of deriving a simple model.

Kjølaas et al. (2022) showed that for the purpose of predicting water droplet concentration profiles in dispersed oil/water flows, the water droplet size distributions could be replaced by the respective Sauter mean values with no significant adverse effects on the accuracy, and an explanation of why this approach works was also supplied.

Using the Sauter mean bubble diameter solves both problems listed above, making the modelling simpler and more efficient. In Fig. 9 we show results obtained when using this simplification on the bubbly flow scenarios presented in this paper. The black lines represent the experimental data, the blue lines represent results obtained with the full model (using the measured droplet size distributions), and the red dashed lines represent results when using the Sauter mean diameters. We observe that the predictions obtained when using the Sauter mean bubble sizes do not differ significantly from the predictions obtained using the full bubble size distributions, which is consistent with the conclusions reached by Kjølaas et al. (2022).

5. Conclusions

In this work we have implemented and tested a gravity-diffusion model for predicting gas concentration profiles in near-horizontal bubbly flow. The motivation for this work is that simple and efficient models for calculating bubbly flow concentration profiles are needed. In particular, for conditions relevant for carbon capture and storage (CCS), bubble entrainment is an important phenomenon that can influence the prevailing flow regime and by extension the frictional pressure loss. Such systems can involve multiphase flow in long pipes, which precludes the use of full 3D models due to the long computational times. A lightweight approach such as the one described here is then needed.

Turbulent diffusion was modelled assuming a homogeneous diffusivity representative of the core diffusivity in single-phase flow. Gravitational drift was modelled using the drag coefficient proposed by Clift and Weber (1988), including non-linear effects of turbulence on the bubble drag. The effect of bubble-bubble hindrance was introduced through the empirical model suggested by Rowe (1987).

Measured bubble sizes were used as input to the model. This allowed us to evaluate the closure laws related to turbulent diffusion and drag, unimpeded by potential uncertainties in the bubble size modelling.

The prevailing model predictions were found to be in good agreement with the measured gas concentration profiles, although there were some discrepancies. It is suspected that the observed discrepancies might be caused by neglecting axial slip between the bubbles and the liquid, as well as the lack of a model coupling the turbulent diffusivity to the presence of gas bubbles.

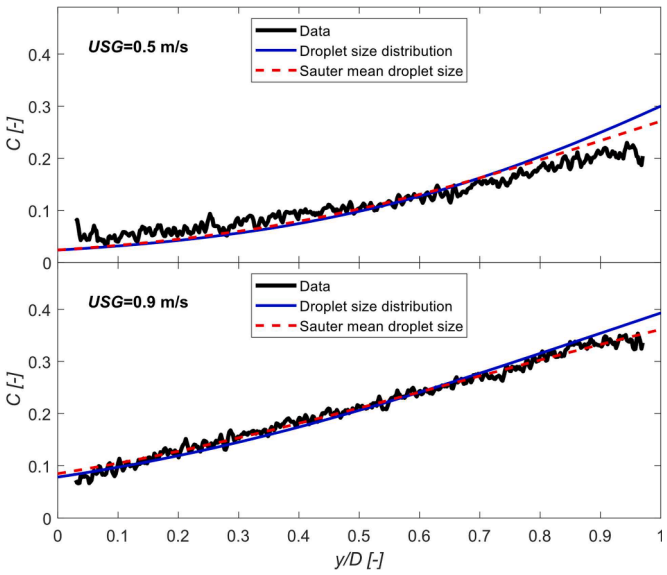

Fig. 9. Examples (USG=0.5 and 0.9 m/s) comparing predictions obtained using the full droplet size distribution (blue solid line) and predictions obtained using the Sauter mean droplet diameter (red dashed line). The black lines represent the measured data.

The results showed that the effect of turbulence on the drag force was crucial to obtain realistic predictions. In fact, omitting this effect caused the predicted gas concentration profile to become much too heterogeneous compared to the measured profiles.

Finally, as Kjølaas et al. (2022) concluded for oil/water dispersions, we found that the Sauter mean bubble size could be used instead of the bubble size distributions without any significant loss of accuracy. This simplification led to significant improvements in the efficiency of the model.

CRediT authorship contribution statement

Jørn Kjølaas: Conceptualization, Methodology, Software, Validation, Investigation, Data curation, Writing – original draft, Writing – review & editing, Visualization. **Diana Gonzalez:** Investigation, Data curation, Writing – review & editing. **Krister Flåten Johansen:** Validation, Investigation, Data curation. **Heiner Schümann:** Investigation, Resources, Data curation, Writing – review & editing, Supervision, Project administration, Funding acquisition.

Declaration of Competing Interest

The authors whose names are listed immediately below certify that they have NO affiliations with or involvement in any organization or entity with any financial interest (such as honoraria; educational grants; participation in speakers' bureaus; membership, employment, consultancies, stock ownership, or other equity interest; and expert testimony or patent-licensing arrangements), or non-financial interest (such as personal or professional relationships, affiliations, knowledge or beliefs) in the subject matter or materials discussed in this manuscript.

Data availability

Data will be made available on request.

Acknowledgments

The work has been conducted as part of ChemFlow, an industry knowledge-building project (NFR project number 314165) financed by

ConocoPhillips, TotalEnergies EP Norge AS, Aker BP, and the Research Council of Norway.

References

Andersen, H., Svendsen, H.E., Solum, S., Yang, Z., Teberikler, L., Solvang, S., Vreenegoor, L., 2021. Experimental study of co2 two-phase flow regime in a large diameter pipe. In: Proceedings of theTCCS-11 - Trondheim Conference on CO2 Capture, Transport and Storage. Trondheim, Norway.

Andreussi, P., Paglianti, A., Silva, F.S., 1999. Dispersed bubble ßow in horizontal pipes. Chem. Eng. Sci. 54, 1101–1107, 54.

Andreussi, P., Paglianti, A., Silva, F.S., 1999. Dispersed bubble flow in horizontal pipes. Chem. Eng. Sci. 54, 1101–1107.

Bottin, M., Berlandis, J., Hervieu, E., Lance, M., Marchand, M., Öztürk, O., Serre, G., 2014. Experimental investigation of a developing two-phase bubbly flow in horizontal pipe. Int. J. Multiphase Flow 60, 161–179.

Clift, R., Weber, M.E., 1988. Bubbles, Drops and Particles. Academic Press, London.

Colin, C., Legendre, D., Fabre, J., 2000. Bubble distribution in a turbulent pipe flow. In: Proceedings of the First Internationnal Symposium on Microgravity Research & Applications in Physical Sciences and Biotechnology. Sorrento, Italy.

Danielson, T.J., Bansal, K.M., Hansen, R., Leporcher, E., 2005. LEDA: The next multiphase flow performance simulator. Proceedings from the 12th International Conference on Multiphase Production Technology. Barcelona, Spain.

Ekambara, K., Sanders, R., Nandakumar, K., Masliyah, J., 2008. CFD simulation of bubbly two-phase flow in horizontal pipes. Chem. Eng. J. 144, 277–288.

Ekambara, K., Sanders, R., Nandakumar, K., Masliyah, J., 2012. CFD modeling of gas-liquid bubbly flow in horizontal pipes: influence of bubble coalescence and breakup. Int. J. Chem. Eng. 2012 https://doi.org/10.1155/2012/620463.

Gidaspow, D., 1994. Multiphase Flow and Fluidization, Continuum and Kinetic Theory Descriptions. Academic Press.

Håland, S., 1983. Simple and Explicit Formulas for the Friction Factor in Turbulent Flow. J. Fluids Eng. ASME 105 (1), 89–90.

Hay, K.J., Liu, Z.C., Hanratty, T.J., 1996. Relation of deposition to drop size when the rate law is nonlinear. Int. J. Multiphase Flow 22 (5), 829–848.

Kenning, V., Crowe, C., 1997. On the effect of particles on carrier phase turbulence in gas-particle flows. Int. J. Multiphase Flow 23 (2), 403–408.

Kjølaas, J., Schümann, H., Gonzalez, D., Johansen, S.T., 2022. Modelling of dispersed oil/water flow in a near-horizontal pipe. Chem. Eng. Sci. 263, 118074.

Kocamustafaogullari, G., Huang, W., 1994. Internal structure and interfacial velocity development for bubbly two-phase flow. Nucl. Eng. Des. 151, 79–101.

Kocamustafaogullari, G., Huang, W., Razi, J., 1994. Measurement and modeling of average void fraction, bubble size and interracial area. Nucl. Eng. Des. 148, 437–453.

Kocamustafaogullari, G., Wang, Z., 1991. An experimental study on local interfacial parameters in a horizontal bubbly two-phase flow. Int. J. Multiphase Flow 17 (5), 553–572.

Laux, H., 1998. Modeling of Dilute and Dense Dispersed Fluid-Particle Two-Phase Flow. Norwegian University of Science and Technology, Trondheim, Norway. PhD dissertation.

Lee, J.C., Meyrick, D.L., 1970. Gas-liquid interfacial areas in salt solutions in an agitated tank. Transactions Inst. Chemical Engr. 48, 37–45.

Lee, M.M., Hanratty, T.J., Adrian, R.J., 1989. The interpretation of droplet deposition measurements with a diffusion model. Int. J. Multiphase Flow 15 (3), 459–469.

Li, C., Yeoh, G.H., Cheung, S.C.P., Tu, J.Y., 2010. Modelling horizontal gas-liquid flow using averaged bubble number density approach. J. Comput. Multiph. Flows 2 (2), 89–99.

Liao, Y., Lucas, D., 2010. A literature review on mechanisms and models for the coalescence process of fluid particles. Chem. Eng. Sci. 65, 2851–2864, 65.

NIST: National Institute of Standards and Technology, 2023 [Online]. Available: http://webbook.nist.gov/chemistry/fluid/.

Pan, L., Hanratty, T.J., 2002. Correlation of entrainment for annular flow in horizontal pipes. Int. J. Multiphase Flow 28, 385–408.

Pourahmadi, F., 1982. Turbulence modeling of single and two phase curved channel flows. University of California, Berkeley ProQuest Dissertations Publishing, Berkeley, USA. PhD dissertation.

Reeks, M.W., 1983. The transport of discrete particles in inhomogeneous turbulence. J. Aerosol Sci. 14 (6), 729–739.

Reichhardt, V.H., 1951. Vollstiindige Darstellung- der turbulenten Geschwindigkeitsverteilung in glatten Leitungen. Z. angew. Math. Mech. 31 (7), 208–219 vol. 31no. 7.

Richardson, J.F., Zaki, W.N., 1954. Sedimentation and fluidisation. Part 1. Trans. Inst. Chem .Eng. 32, 35–53.

Rowe, P.N., 1987. A convenient empirical equation for estimation of the Richardson-Zaki exponent. Chem. Eng. Sci. 42, 2795–2796.

Ruth, D.J., Vernet1, M., Perrard, S., Deike, L., 2021. The effect of nonlinear drag on the rise velocity of bubbles in turbulence. J. Fluid Mech. 924 (A2).

Saffman, P.G., 1965. The lift on a small sphere in a slow shear flow. J. Fluid Mech. 22 (2), 385–400.

Skartlien, R., 2009. A droplet transport model for channel and pipe flow based on particle kinetic theory and a stress–omega turbulence model International. J. Multiphase Flow 35, 603–616.

Skartlien, R., Nuland, S., Amundsen, J.E., 2011. Simultaneous entrainment of oil and water droplets in high Reynolds number gas turbulence in horizontal pipe flow. Int. J. Multiphase Flow 37, 1282–1293.

Sommerfeld, M., 1992. Modeling of particle-wall collisions in confined gas-particle flows. Int. J. Multiphase Flow 18 (6), 905–926.

Tian, Z.F., 2006. Numerical Modelling of Turbulent Gas-Particle Flow and Its Applications. RMIT University.

v. Wachem, B.G.M., Schouten, J.C., Bleek, C.M.V.D., Krishna, R., Sinclair, J.L., 2001. Comparative analysis of CFD models of dense gas–solid systems. AlChE J. 46, 1035–1105.

van Wijngaarden, T., 1976. Hydrodynamic interaction between gas bubbles in liquid. J. Fluid Mech. 77, 27–44.

Yang, Z., 2022. On modeling of CO2 two-phase flow in a near horizontal pipe. In: Proceedings of the 16th International Conference on Greenhouse Gas Control Technologies. Lyon, France.